Idiosyncratic navigation determines mouse CA1 representational structure in a multicompartment environment

Sergio A. Pecirno[1], Alexandra T. Keinath[1]*

[1]Department of Psychology, University of Chicago Illinois, 1007 W Harrison St., Chicago, IL, 60607, USA

*Corresponding author: atk@uic.edu

Organisms from mice to humans rely on cognitive maps instantiated by the hippocampal formation to flexibly and efficiently navigate the world. Traditional theories of cognitive mapping posit that these representations encode geometric relationships among their contents, while recent alternative theories propose that they encode the predictive relationships among their contents that the navigator experiences. Here, we leverage longitudinal miniscope calcium imaging of CA1 in mice navigating a multicompartment environment to adjudicate between predictions of these theories. We find that different mice instantiate different representational structures across identical compartments. Within mouse, compartments with more similar navigational patterns on a particular spatiotemporal scale are represented more similarly, accounting for these individual differences. Finally, we demonstrate that manipulating navigational patterns on this scale induces a corresponding change in CA1 representational structure. Together, these results demonstrate that idiosyncratic navigation is a key determinant of hippocampal representational structure, consistent with predictive theories of cognitive mapping.

In order to survive and thrive, organisms from mice to humans rely on mnemonic representations of the external world and their relationships to it[1]. Referred to as *cognitive maps*, these representations are instantiated by the coordinated activity of spatially-tuned neural populations in the hippocampus and neighboring cortices[2,3]. Classically, cognitive maps are thought to represent geometric relationships – distances and/or angles – among their contents. However, recently proposed alternative theories are challenging this view, positing instead that cognitive maps represent predictive relationships among their contents as experienced by the navigator[4–7]. In many circumstances, both theories arrive at similar predictions, as geometric relationships often determine the predictive relationships between content that the navigator experiences. Nevertheless, there is a fundamental difference between these theories. Geometric theories hold that cognitive maps are determined solely by the relationships among their contents and therefore should be structured similarly across navigators regardless of how they explore a space. Conversely, predictive theories hold that the structure of a navigator's cognitive map is determined at least in part by the way that the navigator explores, and may therefore differ across navigators exploring the same space. Adjudicating between these theories thus carries with it fundamental implications for the nature of cognitive maps and their relationships to behavior.

Within the hippocampus, the structure of the cognitive map is reflected in changes to the firing properties of principal cells that decorrelate the population response when the navigator occupies different spaces, known as *remapping*[8,9]. Prior work has demonstrated that the degree of remapping depends on the features shared between spaces[8–12], past experience with those spaces[13–17], and the broader reference frames in which those spaces are situated[15]. Notably, individual differences in the degree of remapping within the same paradigm have been observed[18], suggesting that remapping is not determined by world features and prior experience alone and can vary between navigators. However, the overwhelming majority of remapping studies rely on manipulations of world features intended to disambiguate spaces. Because of this, it is difficult to know whether the degree of remapping in those paradigms is driven by disambiguating features, or whether remapping instead reflects both featural and navigational differences as implied by predictive theories.

Here we overcome these confounds and directly contrast geometric and predictive theories by characterizing the extent of hippocampal remapping across four identical, connected compartments. By comparing remapping across otherwise identical environments, we can isolate any contribution of idiosyncratic navigational trajectories to representational structure free of confounding featural differences. To do so with high fidelity and across long timescales, we rely on chronic miniscope imaging of hippocampal CA1 in freely navigating mice. We contrast three predictions. If a geometric theory best accounts for the representational structure of CA1, then (i) different mice exploring the same geometric environment should recapitulate similar patterns of remapping across compartments, (ii) this representational structure should not relate to the behavior of the mouse, and (iii) changing a mouse's navigational pattern should not affect this representational structure. On the other hand, if a predictive theory best accounts for the representational structure of CA1, then (i) different mice should exhibit different patterns of remapping across compartments, (ii) each mouse's idiosyncratic representational structure should relate to its idiosyncratic navigational trajectory, and (iii) changing the navigational trajectory of a mouse should change its representational structure to better resemble the new navigational pattern.

In all cases our data supported the predictive claims. Specifically, we found that different mice exhibited different patterns of remapping across compartments which were stable across up to weeks. Within mouse, compartments with more similar navigational trajectories on a second-long timescale during early exploration were represented more similarly by CA1, accounting for

individual differences in representational structure across mice. Finally, modifying the trajectory of the mouse induced a reorganization of the CA1 representational structure to better resemble the structure of the new trajectory, with a reversion to the previous neural and behavioral patterns when this modification was relaxed. Altogether, these results demonstrate that idiosyncratic navigation is a critical determinant of CA1 representational structure, consistent with predictive theories of cognitive mapping.

Results

Characterizing CA1 representational structure in a multicompartment environment

We recorded daily from hippocampal CA1 via miniscope calcium imaging (Fig. 1a) as initially naïve mice (n = 8; 7 male) navigated a radial multicompartment environment (n = 132 sessions). This environment consisted of four 20 cm by 40 cm rectangular compartments connected by a central chamber (Fig. 1b; Mouse 1 explored an alternative version of this environment in which all four compartments were 20 cm by 20 cm squares). Each session lasted either 30, 40, or 60 min depending on imaging signal strength to maximize the amount of data while minimizing the impact of photobleaching. In the first phase of the experiment, mice freely navigated this environment for between four and 15 sessions ($free_1$). In a subset of mice (n = 2), this initial free exploration phase was followed by a phase in which the movement of the mouse was modified. Modification was accomplished by locking the mouse in each compartment for four minutes at a time twice per session, with the mouse freely navigating between compartments in clockwise order when each four-minute epoch ended. Following a week of this limited navigation (*limited*), these mice were returned to free exploration of the environment for three weeks ($free_2$). The environment was not baited with rewards during any phase of the experiment.

For each session, imaging data were first motion corrected[19]. Next, cells were segmented and their calcium traces were extracted via constrained nonnegative matrix factorization (CNMFE; Fig. 1a)[20,21]. For each calcium trace, the likelihood of spiking events which gave rise to that trace were inferred through a second-order autoregressive deconvolution algorithm[22] (OASIS; Fig. 1a). The nonnegative vector this algorithm inferred was treated as the firing rate in all further analyses. Although all mice continued to sample the environment thoroughly throughout the experiment (Fig. S1), to ensure that our results were not driven by differences in the locations sampled within each compartment we subsampled our data to match the spatial sampling distributions between all compartments for all neural analyses (Fig. S2)[23]. Throughout the duration of the experiment, measures of spatial coding quality remained high across populations with most cells meeting traditional place field criteria (Fig. S3). We thus included all cells in all analyses, but note that limiting our analysis to cells meeting traditional place field criteria did not substantially change our results.

Prior work in multicompartment environments has demonstrated that individual CA1 cells tend to be active in multiple compartments[24,25], making comparisons of these representations meaningful. We confirmed this was the case in our data. To do so, for each cell we computed its mean firing rate (MFR) in each compartment, normalized these to the maximum across compartments for each cell, and sorted these normed MFRs from the most active to least active compartments. In all phases of the experiment, CA1 cells remained active in multiple compartments, maintaining normalized MFRs of around 25% of their maximum even in their least active compartments (Fig. 1c). Normalized MFRs were greater during the limited navigation phase than during either free navigation phases, indicating a more equal distribution of firing across compartments during limited navigation (Fig. 1c).

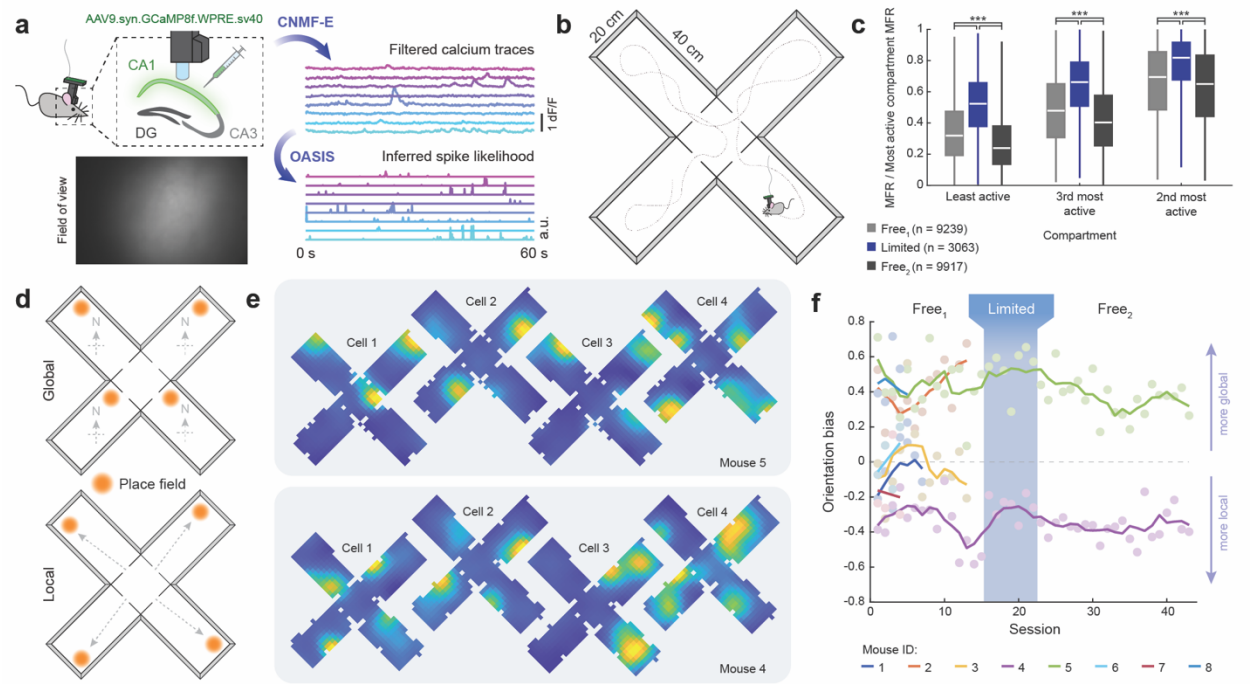

Figure 1. Characterizing mouse CA1 in a multicompartment environment via miniscope imaging. *(a) Schematic of miniscope imaging and data processing pipeline. (b) Schematic of the multicompartment environment. (c) Normalized MFRs as a function of compartment (2nd most active to least active) for all phases of the experiment. (d) Schematic contrasting global and local orientational configurations across compartments in this environment. (e) Representative rate maps of four simultaneously recorded cells from two mice. Each rate map is normalized from zero (blue) to the maximum for that rate map (yellow). (f) Orientational bias for each mouse during each session (dots), as well as the five-session sliding average (lines). All statistical tests and outcomes reported in Supplementary Table 1. ***p<0.001*

Before we can compare navigational trajectories or spatial firing characteristics across compartments, we must determine how to properly orient those compartments. The radial arrangement of compartments in our environment motivates two potential orientational configurations: a *global* configuration where compartments are best aligned by global north, and a *local* configuration where compartments are best aligned by their entry direction (Fig. 1d)[26]. Thus we next asked whether cells in our dataset exhibited evidence of global or local orientational configurations. Examining whole-environment rate maps suggested that cells with both orientational preferences could be seen in our data (Fig. 1e), echoing prior demonstrations of orientational heterogeneity in CA1[27]. To quantify this observation, for each cell we computed 10 x 10 pixel rate maps for each compartment, compressing the long axis of each compartment to make global alignments feasible. Next, we correlated the rate maps between all pairwise comparisons of compartments aligned by both local and global orientations. Finally, we computed the proportion of comparisons for which a global orientation maximized this correlation minus the proportion of comparisons for which a local orientation maximized this correlation, excluding cases which did not produce a good fit (both rs < 0.60) or where firing rates were low (<20% its maximum). This yielded for each cell an orientation score ranging from -1 to +1 indicating the frequency with which a local (-1) or global (+1) orientation maximized across-compartment rate map correlations. Averaging across cells within each mouse, we found that different mice exhibited distinct orientational preferences which persevered across all phases of the experiment

up to 43 days (Fig. 1f). Due to this heterogeneity, for all further cross-compartment comparisons which required alignment of data, we chose the global (n=5) or local (n=3) orientation depending on the mean orientational bias across sessions for each mouse.

Different mice instantiate distinct and persistent patterns of remapping across identical compartments

Having demonstrated that active CA1 cells in our dataset fire promiscuously across compartments and that mice maintain persistent orientational biases, we next addressed our motivating predictions. We began by asking whether the patterns of remapping across compartments were similar across mice, consistent with a geometric theory of cognitive mapping, or differed between mice, consistent with a predictive theory. To do so, for each session in the first free navigation phase of our experiment (n = 76 sessions) we computed the population vector (PV) correlations between all pairwise comparisons of compartment rate maps within each session (Fig. 2a), yielding a matrix that we refer to as the *PV structure*. Next, we correlated these PV structures to one another (Fig. 2b). If the geometric claim is correct, then the PV structures from the same mouse during different sessions should be just as similar to one another as to the PV structures of different mice. On the other hand, if the predictive claim is correct, then the PV structures of each mouse should be more similar to its own structures from other sessions than to the structures of other mice.

Consistent with the predictive theory, comparing the PV structures of the same mouse from different sessions resulted in significantly higher correlations than comparisons across mice (Fig. 2c,d). These across-mouse differences were so reliable that a simple Euclidean distance-based classifier comparing withheld PV structures to the mean PV structure for each mouse could correctly predict mouse identity well above chance (accuracy = 60.53%, chance = 12.5%, p = ~0; binomial test). This reliable structure was present despite the fact that the magnitudes of PV correlation values between compartments were generally low (Fig. 2e)[28]. Lastly, we found no evidence that different mice converged on a more similar structure over time, as if anything across-mouse correlations weakly decreased when comparing later sessions (Fig. 2f).

Like many traditional measures of remapping, PV correlations are rate map-based and therefore rely on assumptions about binning, smoothing, and alignment. To ensure that our findings were not a product of these assumptions, we repeated this analysis using an alternative measure of representational similarity that did not rely on positional information, coactivity similarity[28–30]. Coactivity similarity is motivated by the observation that the structure of a neural representation is reflected in the firing rate correlations among those neurons. If a population of neurons is representing the same content, then they should instantiate the same correlational structure; if the content that they are representing changes, then the correlational structure should also change. Note that this logic holds regardless of whether we have an accurate assumption about what the content being represented is.

We formalized coactivity similarity as follows. First, for each session we computed the correlations between the smoothed firing rate vectors of all pairwise comparisons of cells when the mouse was in each of the four compartments, creating a cells-by-cells coactivity matrix for each compartment (Fig. 2g). Next, we correlated each of these cells-by-cells coactivity matrices with one another, to derive our *coactivity structure*. Finally we correlated these coactivity structures across pairwise comparisons of sessions (Fig. 2h) and compared these correlations within and across mice. The results of this analysis echoed our previous findings. Comparing the coactivity structures of the same mouse on different sessions resulted in significantly higher correlations than comparisons across mice (Fig. 2i,j). Again, these across-mouse differences

were so reliable that a simple Euclidean distance-based classifier comparing withheld coactivity structures to the mean coactivity structure for each mouse could correctly predict mouse identity well above chance (accuracy = 46.05%, chance = 12.5%, p = 1.082e-13; binomial test). As before, if anything across-mouse correlations weakly decreased when comparing later sessions (Fig. 2k). Altogether, these findings demonstrate that CA1 of different mice instantiate distinct and persistent patterns of remapping across compartments in our paradigm, consistent with a predictive theory of cognitive mapping.

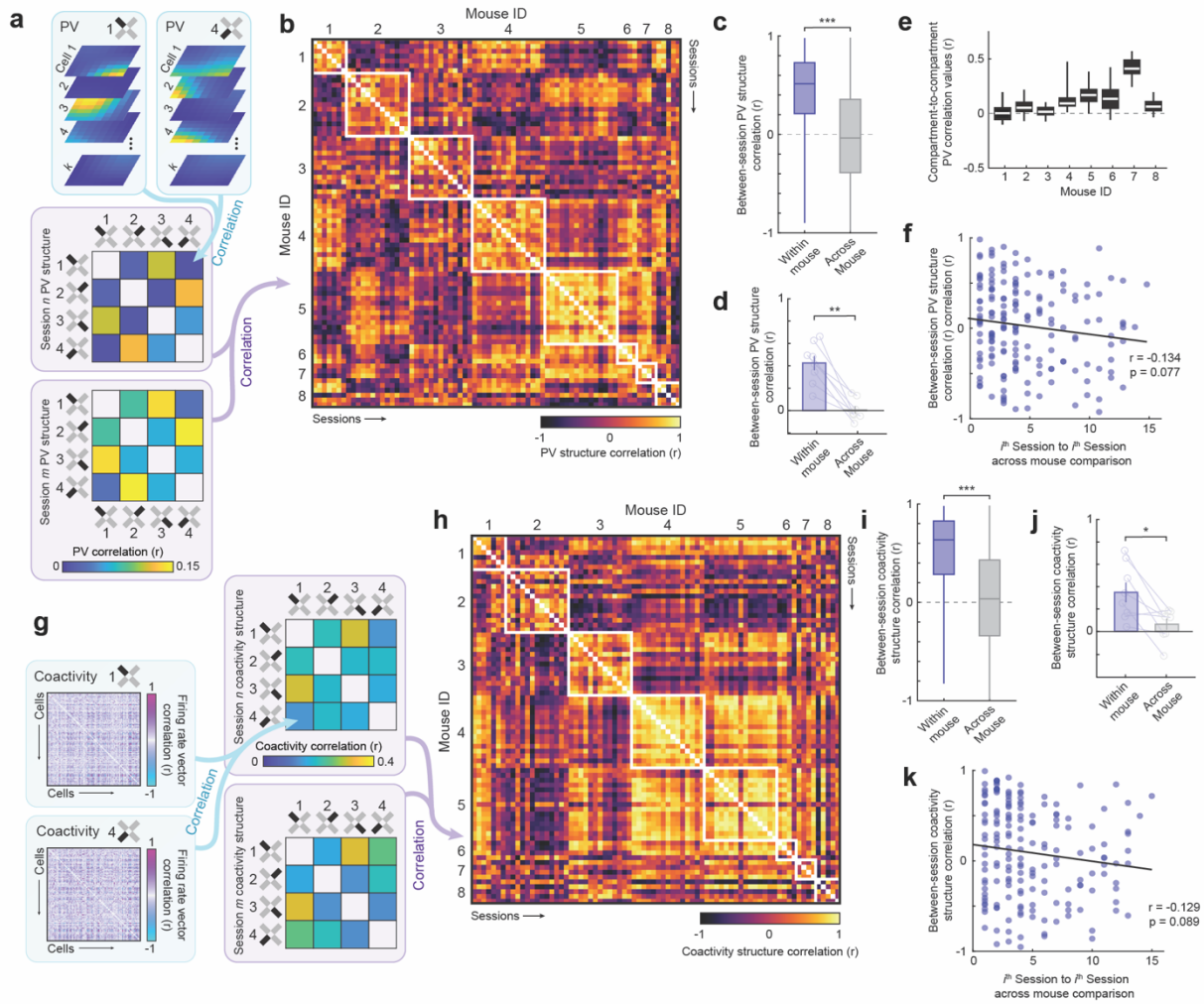

Figure 2. Mice exhibit distinct and persistent patterns of remapping across compartments. *(a) Schematic of PV structure analysis. (b) PV structure correlations across all pairwise comparisons of sessions. White boxes bound sessions from the same mice. (c) PV structure correlations for comparisons within mouse versus across mice, treating each pairwise session comparison independently (rank-sum test: z(867230) = 18.453, p = 4.919e-76). (d) PV structure correlations for comparisons within mouse versus across mice, first averaging for each mouse (signed-rank test: p = 7.812e-03). (e) Distribution of compartment-to-compartment PV correlation values for each mouse. (f) PV structure correlations for the ith session of one mouse to the ith session of another mouse. (g) Schematic of coactivity structure analysis. (h) Coactivity structure correlations across all pairwise comparisons of sessions. White boxes bound sessions from the same mice. (i) Coactivity structure correlations for comparisons within mouse versus across mice treating each pairwise session comparison independently (rank-sum test: z(843720) = 16.927, p*

*= 2.862e-64). (j) Coactivity structure correlations for comparisons within-mouse versus across mice, first averaging for each mouse (signed-rank test: p = 2.344e-02). (k) Coactivity structure correlations for the ith session of one mouse to the ith session of another mouse. *p<0.05, **p<0.01, ***p<0.001*

Idiosyncratic CA1 similarity structures match idiosyncratic patterns of movement during early exploration

Our previous results demonstrate reliable individual differences between mice in CA1 representational structure of our multicompartment environment. While these differences could arise as a result of predictive cognitive mapping, individual differences are not on their own a unique prediction of this theory. The predictive theory does however make a more specific claim: that individual differences in CA1 representational structure should arise as a result of idiosyncratic navigational differences. If correct, then compartments with more similar navigational trajectories should be represented more similarly in our paradigm. We next tested this prediction, again leveraging data from the first free navigation phase of our experiment (n = 76 sessions).

To do so, we operationalized navigational similarity by drawing on a previous formalization of predictive cognitive mapping, the successor representation[4]. At a high level, the successor representation defines the behavioral determinants of hippocampal representational structure as the temporally discounted probabilities of transitioning between locations within an environment. Motivated by this conceptualization, for each session s and compartment k we binned the position data into a 10 x 10 pixel grid of locations (compressing the long axis of each compartment) and computed the proportion of transitions from each pixel to every other pixel after a time lag of n frames (frames recorded at 30Hz; 0.0333 sec step per frame; Fig. 3a). This yielded a 100 x 100 pixel matrix for each lag $n = i$, which we denote ${}_k^sM_i$. We repeated this process for all stepwise time lags from n = 1 to 900, spanning 30 seconds into the future. Next, we computed the exponentially-weighted element-wise sum across these transition matrices such that

$$ {}_k^sM = \sum_{n=1}^{900} {}_k^sM_n e^{(-\gamma n/30)} \tag{1} $$

where the decay constant γ determines the extent to which transitions at longer time lags are discounted (Fig. 3a). This temporal discount factor γ is not known *a priori* but will be estimated from the data. This yields our successor matrix ${}_k^sM$ for session s and compartment k.

This approach allows us to characterize navigational trajectories within each compartment for each session. However, all mice explored the environment for multiple sessions, and it is not obvious whether navigation during every session should have an equal impact on CA1 representational structure. While this is certainly a possibility, it is also possible that more recent behavior or initial behavior has an exaggerated impact on determining CA1 representational structure. The longitudinal nature of our recording paradigm allows us to test these possibilities. To do so, we computed the cumulative successor matrix ${}_k^sC$ for each session s and compartment k as the exponentially-weighted element-wise sum of all matrices ${}_k^iM$ across sessions up to and including $i = s$ such that

$$ {}^{s}_{k}C = \sum_{i=1}^{s} {}^{i}_{k}M e^{(-\tau i)} \tag{2} $$

where the constant τ determines the extent to which each individual session successor matrix contributes to the weighted sum (Fig. 3a). Negative values of τ overweight more recent session matrices, while positive values overweight early session matrices. This constant τ is also not known *a priori* but can be estimated from the data. Finally, we computed the *cumulative successor structure* for session s by correlating ${}^{s}_{k}C$ between all pairwise comparisons of compartments k (Fig. 3a). This approach thus allows us to quantify cumulative navigational similarity with two free parameters, γ and τ.

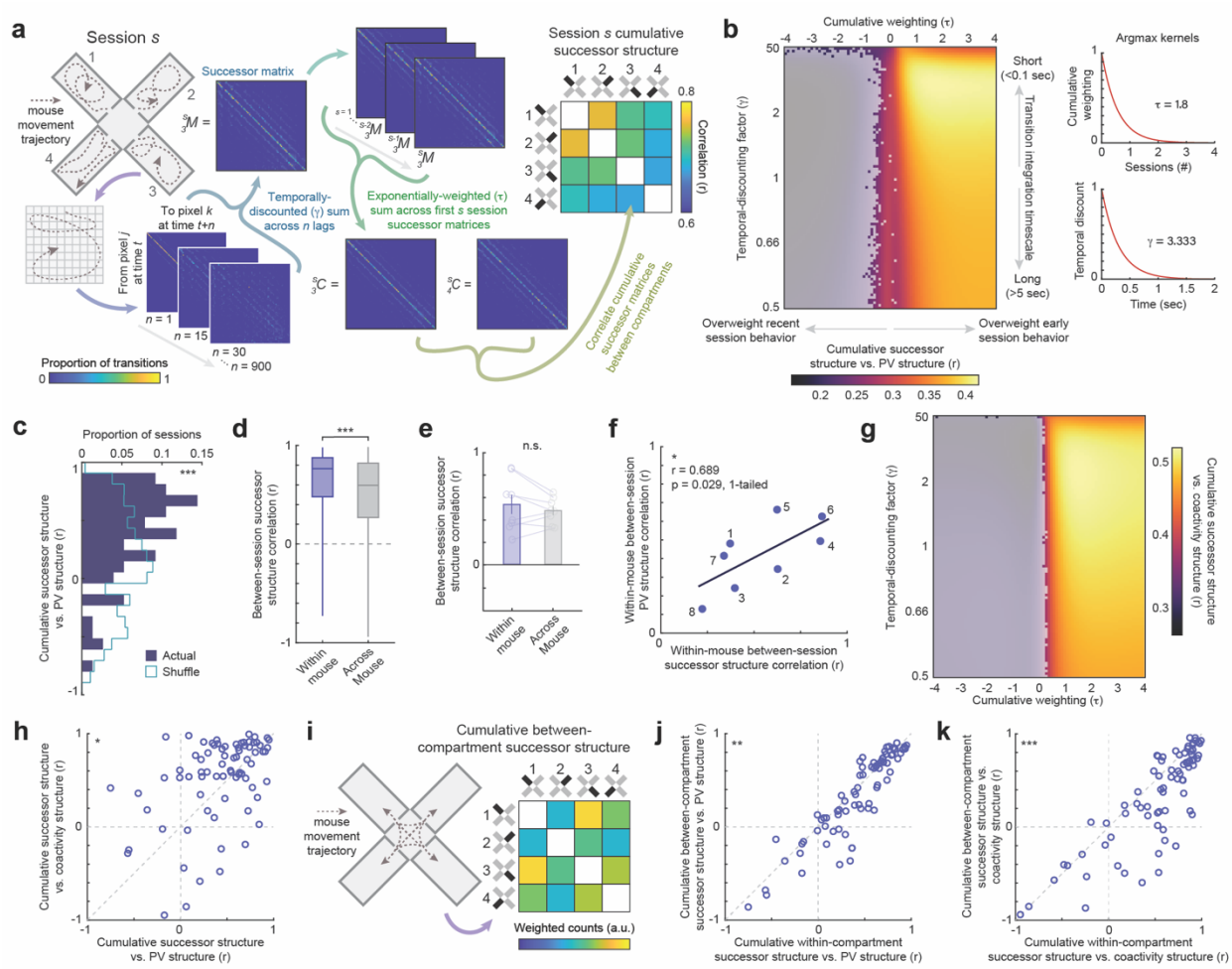

Figure 3. Compartments with similar navigational trajectories during early exploration on a second-long timescale are represented more similarly in mouse CA1. *(a) Schematic for deriving within-compartment cumulative successor structure. (b) Grid search characterizing how γ and τ parameters impact the mean correlation between cumulative successor structure and PV structure. Shaded pixels do not exceed shuffled controls (p>0.001 uncorrected). Kernels reflecting the parameterization which maximizes the correlation between cumulative successor structure and PV structure also shown. (c) Actual correlations between cumulative successor structure and PV structure at the maximizing parameterization for all sessions versus shuffled control (comparison of means across 100,000 shuffles, p = ~0). (d) Correlations of non-cumulative (γ = 3.333) successor structures across sessions for comparisons within mouse versus across mice,*

*treating each pairwise session comparison independently (rank-sum test: z(709074) = 8.184, p = 2.744e-16). (e) Correlations of non-cumulative (γ = 3.333) successor structures across sessions for comparisons within mouse versus across mice, first averaging within each mouse (signed-rank test: p = 0.461). (f) Averaging within-mouse, greater between-session successor structure correlations are associated with greater PV structure correlations. Mouse identity noted. (g) As in (b), except characterizing how γ and τ parameters impact the correlation between cumulative successor structure and coactivity structure. (h) Cumulative successor structure is more highly correlated with coactivity structure than PV structure at argmax parameterizations (signed-rank test: z(985)=2.47, p = 0.013). (i) Schematic for computing cumulative between-compartment successor structure. (j,k) At maximizing parameterizations, cumulative within-compartment successor structure is more highly correlated with both (j) PV structure (signed-rank: z(2025)=2.910, p = 3.618e-03) and (k) coactivity structure (signed-rank: z(2450)=5.110, p = 3.221e-07). *p<0.05, **p<0.01, ***p<0.001*

With this approach, we first tested whether any combination of parameterizations yielded cumulative successor structures which correlated with CA1 PV structures. To do so, we carried out a grid search of combinations of γ and τ. We varied γ from +0.5 to +50 on a log scale, where γ = +50 corresponds to an extremely high temporal discount (i.e. extremely short-timescale (<0.1 sec) transitions dominate the weighted sum) and γ = +0.5 corresponds to an extremely low temporal discount factor (i.e. even long-timescale (>5 sec) transitions contribute to the weighted sum). We also linearly varied τ from -4 to +4, where at τ = -4 the most recent session dominates the weighted sum, at τ = 0 all sessions contribute equally, and at τ = +4 the first session dominates the weight sum. In each case, the resulting cumulative successor structure was computed for each session and correlated with the CA1 PV structure for that session.

This analysis revealed strong correlations between cumulative successor structure and PV structure under many parameterizations (Fig. 3b). While most parameterizations which overweighted early session behavior produced correlations which exceed shuffled controls, this correlation was maximized when paired with a temporal discount factor integrating transitions on a second-long timescale (argmax at γ = 3.333, τ = 1.8; Fig. 3c). Of note, because overweighting early sessions but not current session behavior yielded high correlations with PV structure, it is unlikely that this relationship is driven by low-level within-session confounds. These results thus provide correlational evidence that idiosyncratic navigational trajectories on a second-long timescale during early exploration play a key role in determining CA1 representational structure, consistent with predictive theory claims.

To gain further insight into how behavior on this timescale (γ = 3.333) varied within and across mice, we next computed individual session (non-cumulative) successor structures by correlating ${}^{s}_{k}M$ between all pairwise comparisons of compartments k, and correlated these structures between sessions. Echoing our neural findings (Fig. 2), this analysis revealed that successor structures were generally more consistent within mice than across mice (Fig. 3d). We noted, however, that some mice exhibited more consistency in their successor structures across sessions (Fig. 3e). If CA1 representational structure is determined by consistent successor biases, then one might expect mice with more consistent successor structures across sessions to also exhibit more consistent CA1 representational structures. In line with this prediction, we found that mice with greater between-session successor structure correlations also exhibited greater between-session PV structure correlations (Fig. 3f).

To ensure that the correlation between cumulative successor structure and CA1 PV structure was not the product of the assumptions inherent in PV correlations, we repeated our analysis except comparing cumulative successor structure to coactivity structure. Similar to our

PV results, a grid search across τ and γ again revealed a significantly high correlation between cumulative successor structure and coactivity structure only when overweighting early session behavior and when characterizing movement on a second-long timescale (argmax at γ = 2.381, τ = 1.5; Fig. 3g). Moreover, correlations between cumulative successor structure and coactivity structure actually exceeded the correlations between cumulative successor structure and PV structure at maximizing parameterizations (Fig. 3h). These results indicate that the relationship between successor structure and CA1 representational structure is present across diverse measures of neural similarity.

Finally, we asked whether transitions between compartments, rather than the similarity of trajectories within compartments, could equally well account for CA1 representational structure (Fig. 3i). To this end, we computed the cumulative temporally discounted transitions between compartments and correlated these structures with PV and coactivity structures. We repeated our grid search to arrive at optimal temporal-discounting and cumulative weight values for between-compartment successor structures (argmax for correlation with PV structures: γ = 2.18, τ = 0.4; argmax for correlation with coactivity structures: γ = 1.56, τ = 0.1). Comparing argmax outcomes, we found that between-compartment successor structures resulted in significantly lower correlations with both PV and coactivity structures than within-compartment successor structures (Fig. 3j,k). These results demonstrate that within-compartment successor structure is a unique predictor of CA1 representational structure, which may explain why prior work did not find evidence of between-compartment connectivity reflected in the CA1 representation[31].

Changing patterns of movement induces a corresponding change in CA1 representational structure

Our results so far demonstrate that reliable individual differences in CA1 representational structure are correlated with cumulative successor structure on a second-long timescale, overweighting early session behavior. While these results provide correlational evidence consistent with a predictive theory of cognitive mapping, these theories make a stronger, causal claim. That is, changing the movements of a navigator should induce corresponding changes in representational structure. We next sought to test this prediction. To this end, we followed the initial free navigation phase (*15 sessions; free*$_1$) of the experiment with an additional phase of limited navigation (7 *sessions*; *limited*) and subsequent free navigation (21 *sessions*; *free*$_2$) in two mice exhibiting reliable successor and neural similarity structures (Mouse 4 and Mouse 5). Each limited navigation session consisted of locking the mouse in each compartment for four minutes at a time twice per session, with the mouse freely navigating between compartments in clockwise order when each four-minute epoch ended. Because coactivity similarity required the fewest assumptions, yielded the highest correlations with cumulative successor structure, and was most consistent across sessions in these mice, we focused on this measure of neural similarity in the remaining analyses.

While our manipulation did not force the mice to take a particular navigational trajectory, we reasoned that limiting the navigational options would lead mice to deviate from their free navigational patterns. To confirm this, we first asked whether limited navigation reversibly altered successor structure on the relevant timescale (γ = 2.381, argmax for coactivity similarity) for each mouse. To do so, we again computed individual session (non-cumulative) successor structures by correlating ${}^{s}_{k}M$ between all pairwise comparisons of compartments. We then correlated these matrices between sessions for each mouse. We found that, in both mice, successor structures were more highly correlated within phase and between free$_1$-free$_2$ comparisons than across free-limited comparisons, indicating that our manipulation was successful (Fig. 4a). However, we did observe a difference in post-limited behavior between these two mice. Specifically, Mouse 5

displayed equal correlations within phase and between free$_1$-free$_2$ comparisons indicating complete return to the free$_1$ successor structure following the limited navigation phases. On the other hand, Mouse 4 exhibited lower correlations between free$_1$-free$_2$ comparisons than within phase comparisons, indicating only a partial return to the free$_1$ successor structure. Nevertheless, in both cases limiting navigation induced temporary changes in successor structure on the relevant timescale.

Next, we asked whether our manipulation also impacted CA1 representational structure by correlating coactivity structures between sessions for each mouse (Fig. 4b). Indeed, both mice exhibited changes in coactivity structure during limited navigation which mirrored their changes in successor structure (Fig. 4c). Specifically, in both mice coactivity structure was more highly correlated across within phase and between free$_1$-free$_2$ comparisons than across free-limited comparisons. Mouse 5 displayed equal correlations within phase and between free$_1$-free$_2$ comparisons indicating complete return to the free$_1$ coactivity structure following limited navigation (which persisted even months later, Fig. S4). Mouse 4 exhibited significantly lower correlations between free$_1$-free$_2$ comparisons indicating only a partial return to the free$_1$ coactivity structure. Together, these results demonstrate that changes in CA1 representational structure can be induced by changing navigational trajectories on the relevant timescale, consistent with predictive theory claims.

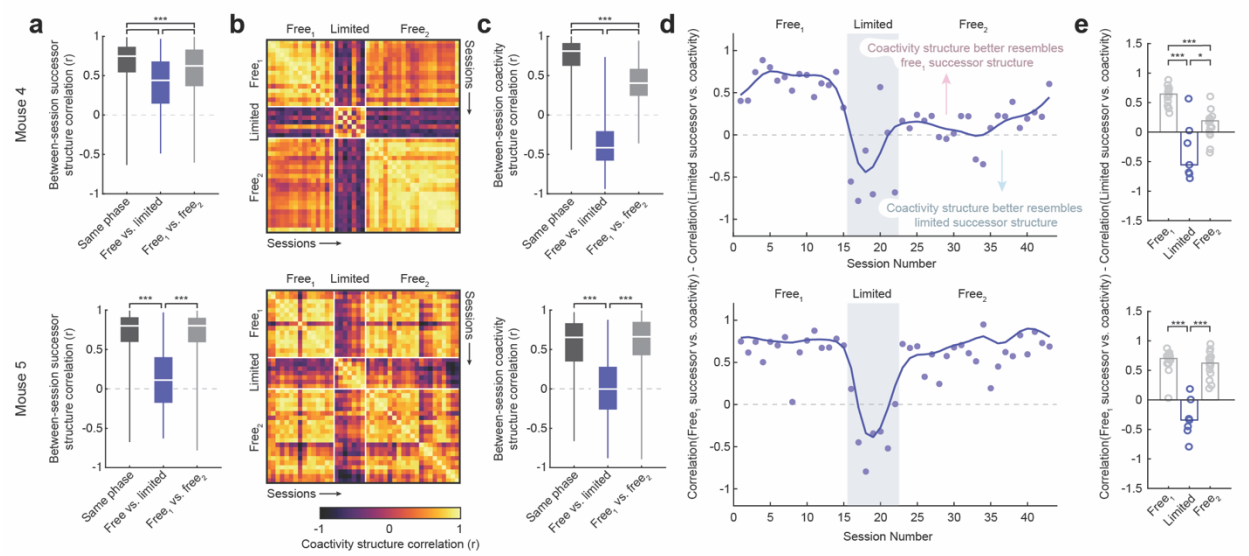

Figure 4. Changing behavior induces a corresponding change to CA1 representational structure. *In all panels, data from Mouse 4 are above and data from Mouse 5 are below. (a) Between-session successor structure correlations when comparisons come from the same phase, between free and limited phases, or across both free phases. (b) Between-session coactivity structure correlations. White lines demarcate changes in experimental phase. (c) Between-session coactivity structure correlations when comparisons come from the same phase, between free and limited phases, or across both free phases. (d) Correlation of the free$_1$ successor structure versus coactivity structure minus the correlation of the limited successor structure versus coactivity structure. Dots denote raw session values, line denotes values when coactivity structure is smoothed across sessions with a gaussian kernel with a standard deviation of two sessions. (e) Raw session values as in (d) except binned by experimental phase. All statistical test information reported in Supplementary Table 2. *p<0.05, p<0.001*

While these results demonstrate coincident changes in successor structure and CA1 representational structure, predictive theories make an additional stronger claim about the relationship between these variables. That is, changes in patterns of navigation should induce changes to representational structure which make the CA1 structure better resemble the new patterns of navigation. We lastly tested this directional prediction. To do so, we computed the mean successor structure for $free_1$ and limited phases. Next, we correlated each of these with the coactivity structure for each session and subtracted the limited correlations from the $free_1$ correlations (Fig. 4d). This yields a measure of the extent to which the coactivity structure for each session better resembles the mean $free_1$ successor structure (if positive) or the mean limited successor structure (if negative). For both mice, this measure demonstrated that coactivity structure changed during limited navigation to better resemble the limited successor structure, and returned to better resemble the $free_1$ successor structure during the subsequent $free_2$ phase (Fig. 4e). Together these results demonstrate that changing patterns of navigation induces a corresponding change of CA1 representational structure to better match the new navigational pattern, consistent with predictive theory claims.

Discussion

Here we leveraged miniscope imaging of mouse CA1 in a multicompartment environment to contrast three claims distinguishing geometric and predictive theories of cognitive mapping. Firstly, using diverse measures of neural similarity which differed in their assumptions, we demonstrated that different mice exhibited distinct patterns of remapping across identical compartments which persisted for weeks[32]. Next, we showed that for each mouse compartments with more similar navigational patterns on a second-long timescale during early exploration exhibited more similar CA1 representations, accounting for these individual differences in representational structure. Finally, we demonstrated that changing the navigational trajectories of the mouse by limiting its options induced a transient change in CA1 representational structure to better resemble the new navigational pattern. In all three cases, these results demonstrate that idiosyncratic navigation at a particular spatiotemporal scale is a key determine of CA1 representational structure, supporting a predictive theory of cognitive mapping in this subregion.

In this experiment, we compared patterns of remapping across identical, unrewarded compartments in order to isolate a potential influence of idiosyncratic navigation on hippocampal representational structure distinct from confounding differences in world features or reward structure. Given that we find evidence of such a determinant under these circumstance, we hypothesize that remapping across environments intentionally disambiguated by external cues[8,13,15,16] reflects both differences in input features as well as idiosyncratic differences in navigation. Likewise, these results provide evidence that predictive structure is an ongoing determinant of CA1 representational structure even in the absence of external rewards. Thus we hypothesize that influences of reward structure on hippocampal coding[33–35] may reflect both differences in rewarding input features as well as differences in goal-directed navigational trajectories.

Our operationalization of navigational similarity was motivated by the successor representation model of hippocampal cognitive mapping[4]. In this model, the hippocampus can be understood as mapping temporally-discounted transitions between states of the world, which can be defined not only by location but also extra-spatial features. Indeed, one of the most compelling successes of this model is the ability to make quantitative predictions across scales (single cells, neural populations, behavior), species (rodents, humans), and domains (physical space, visual spaces, conceptual spaces)[4,36–38]. Although for simplicity we characterize transitions between locations as the representational determinant in this work, we imagine that in practice the CA1

representational structure may be better understood as reflecting transitions among its entorhinal inputs which themselves vary by location[39]. In line with this, we would hypothesize that idiosyncratic trajectories determine CA1 structure when navigating extra-spatial domains, in both rodents and humans. Additionally, we note that the successor representation is not the only theory consistent with a navigational determinant of CA1 representational structure[5–7,40,41]. While our results are consistent with the predictions of this model, our experiment was not designed to adjudicate between competing theories of predictive cognitive mapping.

Our results demonstrate that CA1 representational structure most closely matches successor structure when computed with a second-long temporal discount factor and overweighting early sessions. These characteristics are reminiscent of a unique form of hippocampal plasticity known as behavioral timescale synaptic plasticity (BTSP)[42,43]. BTSP is a mechanism by which new place fields can be endogenously or artificially induced in previously silent CA1 cells by evoking a calcium-mediated plateau potential. Properties of induced place fields indicate that inputs active within a few seconds of this event are potentiated, that these fields exhibit skew which depends on the navigational trajectory during the initial plateau potential, and that endogenous plateau potentials are most common during initial experience[42,44]. It is thus possible that the navigational determinants of CA1 representational structure we characterize here are a product of BTSP, and more generally that BTSP provides a biological basis for the normative claims of predictive mapping theories. If so, then we would expect to observe an increase in plateau potentials not only in novel environments but also during novel experiences which provoke representational change[45]. Possibly consistent with this, we observed a redistribution of firing rates across compartments during limited navigation, coincident with CA1 representational change. However, we interpret this finding with caution due to limitations inherent in our recording technique which do not allow us to distinguish plateau potentials from typical action potentials.

Altogether, our work demonstrates that idiosyncratic navigation is a key determinant of CA1 representational structure in mice, driving individual differences in remapping across identical compartments. These findings are consistent with a predictive theory of cognitive mapping and hold important implications for the ways in which behavior and experience interact to guide the structure of our mnemonic representations.

References

1. Tolman, E. C. Cognitive maps in rats and men. *Psychol Rev* **55**, 189–208 (1948).
2. O'Keefe, J. & Nadel, L. *The Hippocampus as a Cognitive Map*. (Oxford University Press, 1978).
3. McNaughton, B. L., Battaglia, F. P., Jensen, O., Moser, E. I. & Moser, M.-B. Path integration and the neural basis of the 'cognitive map'. *Nat Rev Neurosci* **7**, 663–678 (2006).
4. Stachenfeld, K. L., Botvinick, M. M. & Gershman, S. J. The hippocampus as a predictive map. *Nat Neurosci* **20**, 1643–1653 (2017).
5. George, D. *et al.* Clone-structured graph representations enable flexible learning and vicarious evaluation of cognitive maps. *Nat Commun* **12**, 2392 (2021).
6. Whittington, J. C. R. *et al.* The Tolman-Eichenbaum Machine: Unifying Space and Relational Memory through Generalization in the Hippocampal Formation. *Cell* **183**, 1249-1263.e23 (2020).
7. Levenstein, D., Efremov, A., Eyono, R. H., Peyrache, A. & Richards, B. Sequential predictive learning is a unifying theory for hippocampal representation and replay. Preprint at https://doi.org/10.1101/2024.04.28.591528 (2024).
8. Leutgeb, S. *et al.* Independent codes for spatial and episodic memory in hippocampal neuronal ensembles. *Science* **309**, 619–23 (2005).
9. Bostock, E., Muller, R. U. & Kubie, J. L. Experience-dependent modifications of hippocampal place cell firing. *Hippocampus* **1**, 193–205 (1991).
10. Jeffery, K. J. & Anderson, M. I. Dissociation of the geometric and contextual influences on place cells. *Hippocampus* **13**, 868–72 (2003).
11. Fuhs, M. C., Vanrhoads, S. R., Casale, A. E., McNaughton, B. & Touretzky, D. S. Influence of path integration versus environmental orientation on place cell remapping between visually identical environments. *J Neurophysiol* **94**, 2603–16 (2005).
12. Tanni, S., de Cothi, W. & Barry, C. State transitions in the statistically stable place cell population correspond to rate of perceptual change. *Curr Biol* **32**, 3505-3514.e7 (2022).
13. Bostock, E., Muller, R. U. & Kubie, J. L. Experience-dependent modifications of hippocampal place cell firing. *Hippocampus* **1**, 193–205 (1991).
14. Lever, C., Wills, T., Cacucci, F., Burgess, N. & O'Keefe, J. Long-term plasticity in hippocampal place-cell representation of environmental geometry. *Nature* **416**, 90–4 (2002).
15. Colgin, L. L. *et al.* Attractor-map versus autoassociation based attractor dynamics in the hippocampal network. *J Neurophysiol* **104**, 35–50 (2010).
16. Wills, T. J., Lever, C., Cacucci, F., Burgess, N. & O'Keefe, J. Attractor dynamics in the hippocampal representation of the local environment. *Science* **308**, 873–6 (2005).
17. Plitt, M. H. & Giocomo, L. M. Experience-dependent contextual codes in the hippocampus. *Nat Neurosci* **24**, 705–714 (2021).
18. Nilchian, P., Wilson, M. A. & Sanders, H. Animal-to-Animal Variability in Partial Hippocampal Remapping in Repeated Environments. *The Journal of Neuroscience* **42**, 5268–5280 (2022).
19. Pnevmatikakis, E. A. & Giovannucci, A. NoRMCorre: An online algorithm for piecewise rigid motion correction of calcium imaging data. *J Neurosci Methods* **291**, 83–94 (2017).
20. Pnevmatikakis, E. A. *et al.* Simultaneous Denoising, Deconvolution, and Demixing of Calcium Imaging Data. *Neuron* **89**, 285–99 (2016).
21. Zhou, P. *et al.* Efficient and accurate extraction of in vivo calcium signals from microendoscopic video data. *Elife* **7**, (2018).
22. Friedrich, J., Zhou, P. & Paninski, L. Fast online deconvolution of calcium imaging data. *PLoS Comput Biol* **13**, e1005423 (2017).

23. Keinath, A. T., Epstein, R. A. & Balasubramanian, V. Environmental deformations dynamically shift the grid cell spatial metric. *Elife* **7**, (2018).
24. Spiers, H. J., Hayman, R. M. A., Jovalekic, A., Marozzi, E. & Jeffery, K. J. Place field repetition and purely local remapping in a multicompartment environment. *Cereb Cortex* **25**, 10–25 (2015).
25. Grieves, R. M., Jenkins, B. W., Harland, B. C., Wood, E. R. & Dudchenko, P. A. Place field repetition and spatial learning in a multicompartment environment. *Hippocampus* **26**, 118–134 (2016).
26. Marchette, S. A., Vass, L. K., Ryan, J. & Epstein, R. A. Anchoring the neural compass: coding of local spatial reference frames in human medial parietal lobe. *Nat Neurosci* **17**, 1598–1606 (2014).
27. Lee, I., Yoganarasimha, D., Rao, G. & Knierim, J. J. Comparison of population coherence of place cells in hippocampal subfields CA1 and CA3. *Nature* **430**, 456–9 (2004).
28. Fenton, A. A. Remapping revisited: how the hippocampus represents different spaces. *Nat Rev Neurosci* **25**, 428–448 (2024).
29. Levy, E. R. J. *et al.* A manifold neural population code for space in hippocampal coactivity dynamics independent of place fields. *Cell Rep* **42**, 113142 (2023).
30. Gava, G. P. *et al.* Integrating new memories into the hippocampal network activity space. *Nat Neurosci* **24**, 326–330 (2021).
31. Duvelle, É. *et al.* Hippocampal place cells encode global location but not connectivity in a complex space. *Curr Biol* **31**, 1221-1233.e9 (2021).
32. Keinath, A. T., Mosser, C.-A. & Brandon, M. P. The representation of context in mouse hippocampus is preserved despite neural drift. *Nat Commun* **13**, 2415 (2022).
33. Jarzebowski, P., Hay, Y. A., Grewe, B. F. & Paulsen, O. Different encoding of reward location in dorsal and intermediate hippocampus. *Current Biology* **32**, 834-841.e5 (2022).
34. Sato, M. *et al.* Distinct Mechanisms of Over-Representation of Landmarks and Rewards in the Hippocampus. *Cell Rep* **32**, 107864 (2020).
35. Gauthier, J. L. & Tank, D. W. A Dedicated Population for Reward Coding in the Hippocampus. *Neuron* **99**, 179-193.e7 (2018).
36. Momennejad, I. *et al.* The successor representation in human reinforcement learning. *Nat Hum Behav* **1**, 680–692 (2017).
37. de Cothi, W. *et al.* Predictive maps in rats and humans for spatial navigation. *Current Biology* **32**, 3676-3689.e5 (2022).
38. Garvert, M. M., Saanum, T., Schulz, E., Schuck, N. W. & Doeller, C. F. Hippocampal spatio-predictive cognitive maps adaptively guide reward generalization. *Nat Neurosci* **26**, 615–626 (2023).
39. de Cothi, W. & Barry, C. Neurobiological successor features for spatial navigation. *Hippocampus* **30**, 1347–1355 (2020).
40. Savelli, F. & Knierim, J. J. Origin and role of path integration in the cognitive representations of the hippocampus: computational insights into open questions. *J Exp Biol* **222**, (2019).
41. Zutshi, I. *et al.* Hippocampal neuronal activity is aligned with action plans. Preprint at https://doi.org/10.1101/2024.09.05.611533 (2024).
42. Bittner, K. C., Milstein, A. D., Grienberger, C., Romani, S. & Magee, J. C. Behavioral time scale synaptic plasticity underlies CA1 place fields. *Science* **357**, 1033–1036 (2017).
43. Milstein, A. D. *et al.* Bidirectional synaptic plasticity rapidly modifies hippocampal representations. *Elife* **10**, (2021).
44. Madar, A. D., Dong, C. & Sheffield, M. E. J. BTSP, not STDP, Drives Shifts in Hippocampal Representations During Familiarization. *bioRxiv* (2023) doi:10.1101/2023.10.17.562791.

45. Monaco, J. D., Rao, G., Roth, E. D. & Knierim, J. J. Attentive scanning behavior drives one-trial potentiation of hippocampal place fields. *Nat Neurosci* **17**, 725–31 (2014).
46. Pnevmatikakis, E. A. & Giovannucci, A. NoRMCorre: An online algorithm for piecewise rigid motion correction of calcium imaging data. *J Neurosci Methods* **291**, 83–94 (2017).
47. Pnevmatikakis, E. A. *et al.* Simultaneous Denoising, Deconvolution, and Demixing of Calcium Imaging Data. *Neuron* **89**, 285–99 (2016).
48. Mathis, A. *et al.* DeepLabCut: markerless pose estimation of user-defined body parts with deep learning. *Nat Neurosci* **21**, 1281–1289 (2018).
49. Skaggs, W. E., McNaughton, B. L. & Gothard, K. M. An information-theoretic approach to deciphering the hippocampal code. in *Advances in neural information processing systems* 1030–1037 (1993).

Methods

Subjects

Eight naive mice (C57Bl/6, Charles River; 7 male, 1 female) were housed in pairs in 20 cm x 40 cm cages which included running wheels and additional enrichment. Mice were kept on a 14-hour light/10-hour dark cycle at 23°C and 30% humidity with food and water ad libitum. All experiments were carried out during the light portion of the light/dark cycle, and in accordance with University of Illinois Chicago Animal Use and Care Committee (protocol #23008) and with AAALAC guidelines.

Surgeries

During all surgeries, mice were anesthetized via inhalation of a combination of oxygen and 5% Isoflurane before being transferred to the stereotaxic frame (David Kopf Instruments), where anesthesia was maintained via inhalation of oxygen and 0.5-2.5% Isoflurane for the duration of the surgery. Body temperature was maintained with a heating pad and eyes were hydrated with gel (Optixcare). Meloxicam (2 mg kg^{-1}) and saline (0.5 ml) were administered subcutaneously at the beginning of each surgery. Preparation for recordings involved three surgeries per mouse.

First, at the age of six to ten weeks, each mouse was transfected with a 400 nl injection of the calcium reporter GCaMP8f via the viral construct AAV9.syn.GCaMP8f.WPRE.SV40 with an original titre of 2.3 x 10^{13} GC ml^{-1} (Addgene) diluted at a 1 part virus to 7 parts sterile artificial cerebrospinal fluid before surgical microinjection.

Three weeks post-injection, a 1.8mm diameter gradient refractive index (GRIN) lens (Go!Foton) was implanted above dorsal CA1 (Referenced to bregma: ML = 2.0 mm, AP = -2.1 mm; Referenced to brain surface: DV = -1.35 mm). Implantation required aspiration of intervening cortical tissue. In addition to the GRIN lens, two stainless steel screws were threaded into the skull above the contralateral hippocampus and prefrontal cortex to stabilize the implant. Dental cement (C&B Metabond) was applied to secure the GRIN lens and anchor screws to the skull. A silicone adhesive (Kwik-Sil, World Precision Instruments) was applied to protect the top surface of the GRIN lens until the next surgery.

Three weeks after lens implantation, an aluminum baseplate was affixed via dental cement (C&B Metabond) to the skull of the mouse, which would later secure the miniaturized fluorescent endoscope (miniscope) in place during recording. The miniscope/baseplate was mounted to a stereotaxic arm for lowering above the implanted GRIN lens until the field of view contained visible cell segments and dental cement was applied to affix the baseplate to the skull. A polyoxymethylene cap was affixed to the baseplate when the mice were not being recorded to protect the baseplate and lens.

After surgery, animals were continuously monitored until they recovered. For the initial two days after surgery mice were provided with additional doses of meloxicam for pain management. One week following baseplating, to familiarize mice with the recording procedure and to monitor the quality of cell activity, we recorded mice daily in a 75 cm x 75 cm square open field for 10 min to 30 min per day. When recording quality was deemed of sufficiently high quality based on a stable number of cells across days, rapid transients, and a high proportion of cells with stable place fields within day (>50% of cells versus shuffled controls), mice began the multicompartment experiment. Mice typically met these criteria 2+ weeks following baseplating.

Apparatus

The recording environment was constructed of white Lego base and white acrylic walls (Professional Plastics). All walls had a height of 20 cm. All compartments were 20 cm x 40 cm, with a 20cm central chamber, except for one mouse for whom all compartments were 20 cm x 20 cm. No symmetry-breaking internal directional cues were provided, but the apparatus was closer to one external grey room wall which could serve as an external directional cue. During recording, the environment was dimly lit by an LED lamp positioned to reduce shadows, and a white-noise machine was used to mask any uncontrolled sounds. All sessions were 30 or 40 min (depending on signal strength to minimize photobleaching), and only one session was recorded per day. On rare occasions (~3%) sessions were impacted by equipment failures, and sessions were terminated early; data from these sessions were not analyzed. During all free exploration sessions, mice were placed in the center of the environment at the start of the session. During limited navigation sessions, mice were placed in the first room at the start of the session. The recording environment was cleaned between recordings with veterinarian-grade disinfectant.

Data acquisition

In vivo calcium videos were recorded with a UCLA miniscope (v3; miniscope.org) containing a monochrome CMOS imaging sensor (MT9V032C12STM, ON Semiconductor) connected to a custom data acquisition (DAQ) box (miniscope.org) with a lightweight, flexible coaxial cable. The DAQ was connected to a PC with a USB 3.0 SuperSpeed cable and controlled with Miniscope custom acquisition software (miniscope.org; software version v4). The outgoing excitation LED was set to between 5-30%, depending on the mouse to maximize signal quality with the minimum possible excitation light to mitigate the risk of photobleaching. Gain was adjusted to match the dynamic range of the recorded video to the fluctuations of the calcium signal for each recording to avoid saturation. Behavioral video data were recorded by a webcam mounted above the environment. The DAQ simultaneously acquired behavioral and cellular imaging streams at 30 Hz as FFV1 losslessly-compressed AVI files and all recorded frames were timestamped for post-hoc alignment.

Data preprocessing

Calcium imaging data were preprocessed prior to analyses via a pipeline of open source MATLAB (MathWorks; version R2024a) functions to correct for motion artifacts[46], segment cells and extract transients[47]. The motion-corrected calcium imaging data were manually inspected to ensure that motion correction was effective and did not introduce additional artifacts. Following this preprocessing pipeline, the spatial footprints of all cells were manually verified to remove lens artifacts. Finally, to estimate the spike trains which gave rise to the transients we recorded, we implemented a second-order autoregressive deconvolution algorithm[22]. The nonnegative vector this algorithm inferred was treated as the firing rate in all further analyses.

Position data were inferred from behavioral videos via DeepLabCut[48] tracking the nose, ears, and tail base of the mouse. The average between the two ears was taken as the position of the mouse in all analyses. Periods were estimates of either ear positions were low-confidence (<0.90) or the estimated distance between the ears was unrealistic (<0.5 cm or >3.5 cm) were excluded and position was linearly interpolated across these timepoints (<1% of timepoints). Position data were then resampled via linear interpolation based on system clock timestamping to estimate the position at each time when imaging frames were collected.

Data analysis

All analyses were conducted using the nonnegative spike train estimates inferred via a second-order autoregressive deconvolution, henceforth the *firing rate* vector. Similar results were observed when binarizing the filtered traces according to the rising phase of the calcium transient. As code quality remained high, we included all cells in all analyses. Including only cells which meet traditional criteria to be classified as place cells, such as high spatial information content and split-half correlations, yielded similar results.

Whole-environment rate maps for each cell were computed by dividing the environment into 2.5 cm x 2.5 cm pixels. Compartment rate maps were computed by first compressing each compartment along its long axis to a 1:1 aspect ratio, and then dividing the compartment into a 10 pixel x 10 pixel grid (equivalent to a 2 cm x 4 cm anisotropic pixelation). Then, to correct for biases in sampled spatial locations, we subsampled our data during all rate map comparisons to match the spatial sampling distributions across compartments[23]. To do so, we computed the minimum number of samples recorded at each pixel location across all compartments (Fig. S2). Next for each comparison we included a random subset of the data recorded at each pixel location to match that minimum number of samples. On the basis of these subsampled data, we computed the mean firing rate for each pixel and then smoothed this map with a 1 pixel standard deviation isometric Gaussian kernel. After smoothing, rate maps were corrected to reduce edge artifacts introduced by smoothing.

Population vector correlations across compartments were computed by concatenating the linearized compartment rate maps of all cells from each compartment and computing the correlation between these vectors. This measure of similarity takes into account both changes in the spatial distributions of firing and relative changes in firing rate.

Coactivity structure was computed by first smoothing the firing rate vectors of each cell with a 1 second standard deviation gaussian kernel. Next, a subset of timepoints when the mouse was in each compartment were selected to match the spatial sampling distributions across all compartments. On the basis of these subsampled data we computed the correlations between all pairwise comparisons of cells within each compartment. Finally, we correlated these matrices between pairwise comparisons of compartments to derive the coactivity structure. This measure is agnostic to the content of the neural code, and is only sensitive to relative changes in the correlations of firing among neurons.

Successor structure and cumulative successor structure were computed as described in the main text. Each session was treated independently when correlating successor structures and neural similarity structures unless otherwise noted. To establish significance, correlation values were compared to a shuffled control where successor structures were randomly permuted across sessions 1000 times.

Split-half correlations were computed for each cell from the whole-environment rate maps by dividing the session data into first vs. second half, computing the rate map for each half (while matching sampling distributions), and correlating the pixel values of these rate maps. The significance of this correlation was determined for each cell by comparing this value to a shuffled control where this procedure was repeated after circularly shifting the position data relative to the firing rate vector a random amount at least 30 sec away from the true alignment. This procedure was iterated 500 times, and the proportion of times the shuffled distribution met or exceeded the actual value was taken as the resulting p-value.

Spatial information content (SIC) was computed from the whole-environment rate maps of each cell as described previously[49] via the equation:

$$\mathrm{SIC} = \sum_{i} \mathbf{p}_i \mathbf{r}_i \log\left(\frac{\mathbf{r}_i}{\bar{\boldsymbol{r}}}\right) \tag{3}$$

where i is the rate map pixel index, $\mathbf{p}_i$ is the probability of sampling pixel i, $\mathbf{r}_i$ is the mean firing rate at pixel i, and $\bar{\mathbf{r}}$ is the mean firing rate across all pixels.

Histological validation of expression and recording targets

After experiments, animals were perfused to verify GRIN lens placement. Mice were deeply anesthetized and intracardially perfused with 4% paraformaldehyde in PBS. Brains were dissected and post-fixed with the same fixative. Coronal sections (50 μm) of the entire hippocampus were cut using a vibratome and sections were mounted directly on glass slides. Sections were split and half of all sections were stained for DAPI and mounted with Fluoromount-G (Southern Biotechnology) to localize GRIN lens placement and to evaluate viral expression. Due to the large imageable surface but restricted miniscope field of view (~0.5 mm x ~0.8 mm), we were unable to determine more specific localization of populations within the hippocampus for mice recorded with 1.8 mm lenses.

Statistics and reproducibility

All statistical tests are noted where the corresponding results are reported throughout the main text and supplement. All tests were uncorrected 2-tailed tests unless otherwise noted. Z-values for nonparametric rank-sum and signed-rank tests were not estimated or reported for comparisons with fewer than 15 datapoints. Box plots portray the minimum and maximum (whiskers), upper and lower quartiles (boxes), and median (cinch/bolded line). All correlations are Pearson's correlations unless otherwise noted.

Code availability

All custom code written for reported analyses are publicly available at [insert Github link] or via request to the corresponding authors.

Data availability

The complete dataset for all experiments are publicly available at [insert Dryad link] or via request to the corresponding authors.

Acknowledgements

This work was supported by startup funding provided by the University of Illinois Chicago, as well as a UIC LAS CSSR seed grant. We would also like to thank J. Quinn Lee and Rachel Donka for feedback when drafting this manuscript.

Author Contributions

SAP and ATK contributed to experimental design, surgeries, recordings, analysis of data, as well as revising the manuscript. ATK drafted the manuscript.

Competing interests.

The authors declare no competing interests.

Supplementary information for:

Idiosyncratic navigation determines mouse CA1 representational structure in a multicompartment environment

Pecirno, et al.

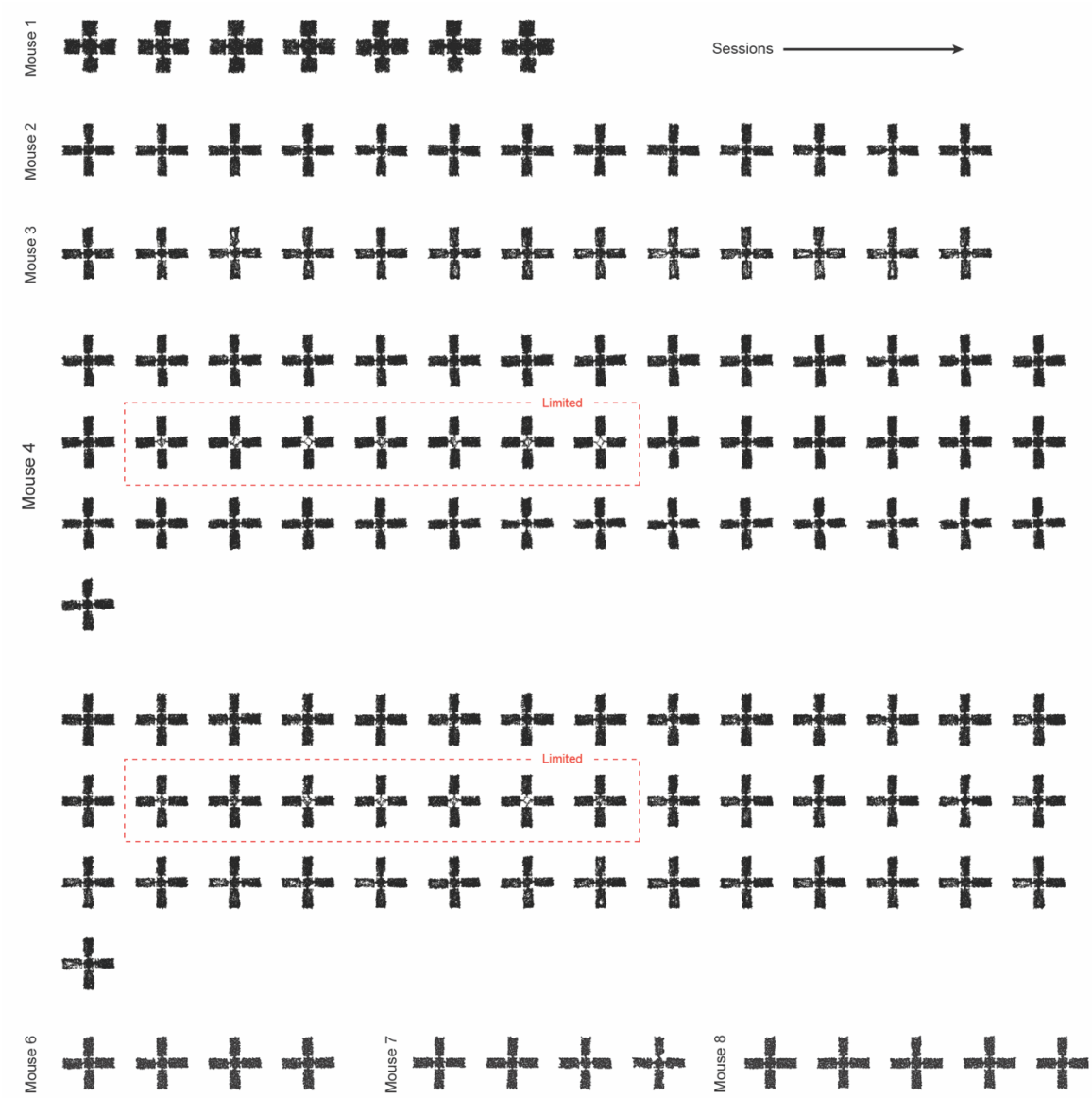

Supplementary Figure 1. Sampling from all mice from all sessions. *For Mouse 4 and Mouse 5, limited navigation sessions are marked by the red dashed box. Mouse 1 navigated an alternative version of this environment where each compartment was 20 cm x 20 cm. All other mice explored the version of this environment where each compartment was 20 cm x 40 cm.*

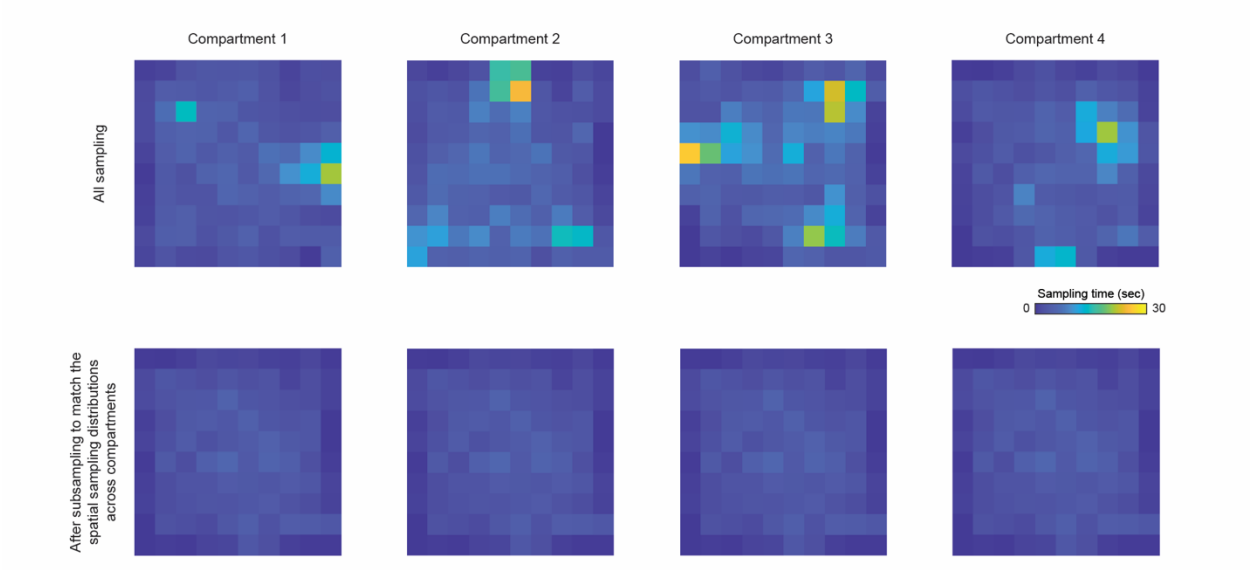

Supplementary Figure 2. Subsampling data to match the spatial sampling distributions across all compartments prior to neural analyses. *Before all neural analyses, a random subset of datapoints within each compartment was chosen such that the resulting spatial sampling distributions were matched across compartments. Because of between-mouse heterogeneity in alignment configuration across compartments (Fig. 1), sampling distributions were aligned according to the orientation configuration for each mouse prior to subsampling. Subsampling was used prior to computing all neural analyses, including coactivity similarity measures. Comparable results were observed when including all data, but this procedure provides additional confidence that the results we obtain are not driven by differences in sampled locations across compartments.*

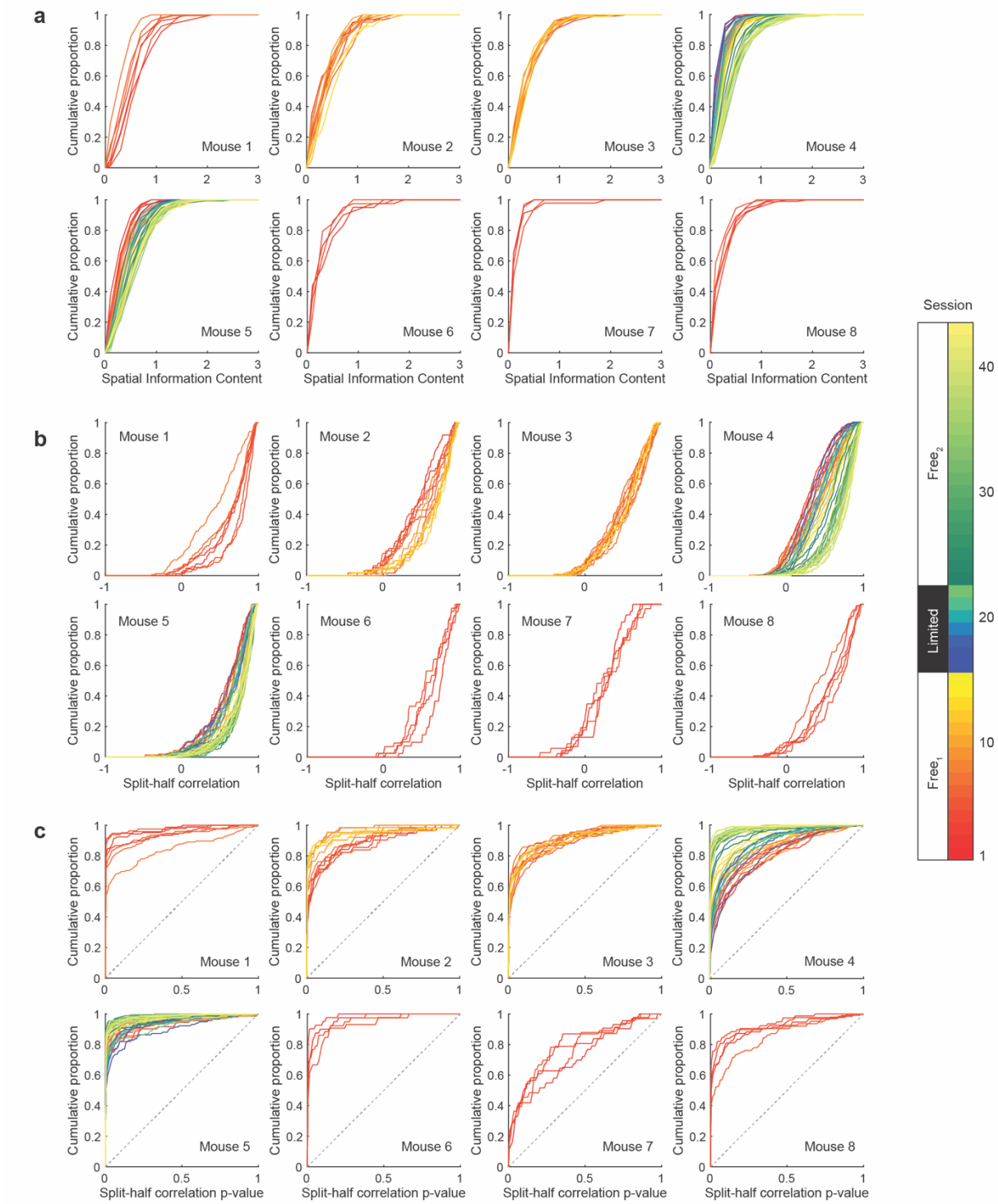

Supplementary Figure 3. Measures of place code quality across the experiment. *(a) Cumulative distribution of spatial information content values across the population for each session and mouse. (b) Cumulative distribution of split half correlations across the population for each session and mouse. (c) Cumulative distribution of the p-values of the split-half correlation values against a shuffled control across the population for each session and mouse.*

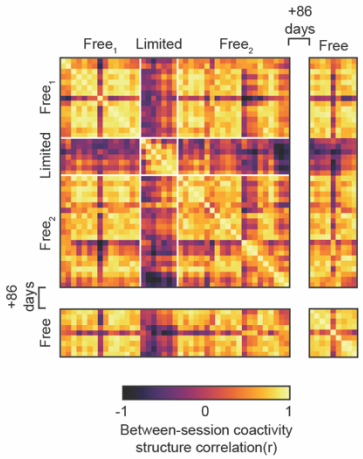

Supplementary Figure 4. Representational structure remains stable across months of unrelated experience. *Because he remained viable for imaging, Mouse 5 was returned to the environment to freely navigate for 9 more sessions beginning 86 days after the main experiment was concluded. During the intervening time he participated in other daily imaging paradigms, with a few weeks of rest in the home cage. Returning him to the environment continued to elicit the same free coactivity structure even after all this time and experience, demonstrating the persistence of these idiosyncratic representational structures.*

Mean firing rate analyses				
Figure panel	Condition	Comparison	Statistical test	Outcome
1c	Least active compartment	$Free_1$ vs. limited	Rank-sum	p = 0.000e+00, Z(50051247)=39.819
1c	Least active compartment	$Free_1$ vs. $Free_2$	Rank-sum	p = 2.718e-154, Z(98615839)=26.461
1c	Least active compartment	$Free_2$ vs. limited	Rank-sum	p = 2.718e-154, Z(98615839)=26.461
1c	2nd least active compartment	$Free_1$ vs. limited	Rank-sum	p = 7.029e-249, Z(51094446)=33.694
1c	2nd least active compartment	$Free_1$ vs. $Free_2$	Rank-sum	p = 1.234e-77, Z(95628946)=18.651
1c	2nd least active compartment	$Free_2$ vs. limited	Rank-sum	p = 0.000e+00, Z(28098846)=45.338
1c	2nd most active compartment	$Free_1$ vs. limited	Rank-sum	p = 9.318e-136, Z(52609694)=24.798
1c	2nd most active compartment	$Free_1$ vs. $Free_2$	Rank-sum	p = 4.915e-18, Z(91806001)=8.655
1c	2nd most active compartment	$Free_2$ vs. limited	Rank-sum	p = 6.321e-209, Z(25471887)=30.846

Supplementary Table 1. Statistical information from analyses presented in Figure 1.

Figure 4 analyses				
Figure panel	Mouse	Comparison	Statistical test	Outcome
1a	4	Same phase vs. Free to Limited	Rank-sum	p = 1.380e-22, z(118889)=9.779
1a	4	Limited vs. $Free_1$ to $Free_2$	Rank-sum	p = 1.601e-08, z(60615)=5.650
1a	4	Same phase vs. $Free_1$ to $Free_2$	Rank-sum	p = 1.171e-05, z(120047)=4.383
1a	5	Same phase vs. Free to Limited	Rank-sum	p = 2.028e-53, z(130319)=15.386
1a	5	Limited vs. $Free_1$ to $Free_2$	Rank-sum	p = 5.498e-54, z(41580)=15.470
1a	5	Same phase vs. $Free_1$ to $Free_2$	Rank-sum	p = 9.736e-01, z(109456)=0.033
1c	4	Same phase vs. Free to Limited	Rank-sum	p = 1.276e-90, z(140106)=20.187
1c	4	Limited vs. $Free_1$ to $Free_2$	Rank-sum	p = 9.191e-77, z(35623)=18.544
1c	4	Same phase vs. $Free_1$ to $Free_2$	Rank-sum	p = 4.683e-54, z(146660)=15.481
1c	5	Same phase vs. Free to Limited	Rank-sum	p = 4.398e-49, z(128973)=14.726
1c	5	Limited vs. $Free_1$ to $Free_2$	Rank-sum	p = 2.498e-52, z(42060)=15.223
1c	5	Same phase vs. $Free_1$ to $Free_2$	Rank-sum	p = 3.068e-01, z(107085)=1.022
1e	4	$Free_1$ vs. Limited	Rank-sum	p = 9.228e-04, z(220)=3.313
1e	4	$Free_1$ vs. $Free_2$	Rank-sum	p = 1.486e-06, z(428)=4.813
1e	4	Limited vs. $Free_2$	Rank-sum	p = 1.466e-02, z(55)=2.441
1e	5	$Free_1$ vs. Limited	Rank-sum	p = 3.244e-04, z(224)=3.595
1e	5	$Free_1$ vs. $Free_2$	Rank-sum	p = 1.235e-01, z(326)=1.540
1e	5	Limited vs. $Free_2$	Rank-sum	p = 1.075e-04, z(28)=3.873

Supplementary Table 2. Statistical information from analyses presented in Figure 4.